



LAWRENCE
LIVERMORE
NATIONAL
LABORATORY

Dust Studies in DIII-D and TEXTOR

D. L. Rudakov, A. Litnovsky, W. P. West, J. H. Yu, J. A. Boedo, B. D. Bray, S. Brezinsek, N. H. Brooks, M. E. Fenstermacher, M. Groth, E. M. Hollmann, A. Huber, A. W. Hyatt, S. I. Krasheninnikov, C. J. Lasnier, R. A. Moyer, A. Yu. Pigarov, V. Philipps, A. Pospieszczyk, R. D. Smirnov, J. P. Sharpe, W. M. Solomon, J. G. Watkins, C. P. C. Wong

February 18, 2009

22nd IAEA Fusion Energy Conference
Geneva, Switzerland
October 13, 2009 through October 18, 2009

Disclaimer

This document was prepared as an account of work sponsored by an agency of the United States government. Neither the United States government nor Lawrence Livermore National Security, LLC, nor any of their employees makes any warranty, expressed or implied, or assumes any legal liability or responsibility for the accuracy, completeness, or usefulness of any information, apparatus, product, or process disclosed, or represents that its use would not infringe privately owned rights. Reference herein to any specific commercial product, process, or service by trade name, trademark, manufacturer, or otherwise does not necessarily constitute or imply its endorsement, recommendation, or favoring by the United States government or Lawrence Livermore National Security, LLC. The views and opinions of authors expressed herein do not necessarily state or reflect those of the United States government or Lawrence Livermore National Security, LLC, and shall not be used for advertising or product endorsement purposes.

Dust Studies in DIII-D and TEXTOR

D.L. Rudakov 1), A. Litnovsky 2), W.P. West 3), J.H. Yu 1), J.A. Boedo 1), B.D. Bray 3), S. Brezinsek 2), N.H. Brooks 3), M.E. Fenstermacher 4), M. Groth 4), E.M. Hollmann 1), A. Huber 2), A.W. Hyatt 3), S.I. Krasheninnikov 1), C.J. Lasnier 4), R.A. Moyer 1), A.Yu. Pigarov 1), V. Philipps 2), A. Pospieszczyk 2), R.D. Smirnov 1), J.P. Sharpe 5), W.M. Solomon 6), J.G. Watkins 7), and C.P.C. Wong 3)

1) University of California, San Diego, La Jolla, California 92093-0417, USA

2) Institut für Energieforschung-Plasmaphysik, Forschungszentrum Jülich, Association EURATOM-FZJ, 52425 Germany

3) General Atomics, P.O. Box 85608, San Diego, California 92186-5608, USA

4) Lawrence Livermore National Laboratory, Livermore, California 94551, USA

5) Idaho National Engineering and Environmental Laboratory, Fusion Safety Program, Idaho Falls, Idaho 83415, USA

6) Princeton Plasma Physics Laboratory, Princeton, New Jersey, USA

7) Sandia National Laboratories, Albuquerque, New Mexico 87185, USA

e-mail contact of main author: rudkov@fusion.gat.com

Abstract. Studies of naturally occurring and artificially introduced carbon dust are conducted in DIII-D and TEXTOR. In DIII-D, dust does not present operational concerns except immediately after entry vents. Submicron sized dust is routinely observed using Mie scattering from a Nd:Yag laser. The source is strongly correlated with the presence of Type I edge localized modes (ELMs). Larger size (0.005-1 mm diameter) dust is observed by optical imaging, showing elevated dust levels after entry vents. Inverse dependence of the dust velocity on the inferred dust size is found from the imaging data. Direct heating of the dust particles by the neutral beam injection (NBI) and acceleration of dust particles by the plasma flows are observed. Energetic plasma disruptions produce significant amounts of dust. Large flakes or debris falling into the plasma may result in a disruption. Migration of pre-characterized carbon dust is studied in DIII-D and TEXTOR by introducing

EX/9-3

micron-size dust in plasma discharges. In DIII-D, a sample holder filled with ~30 mg of dust is introduced in the lower divertor and exposed to high-power ELMing H-mode discharges with strike points swept across the divertor floor. After a brief exposure (~0.1 s) at the outer strike point, part of the dust is injected into the plasma, raising the core carbon density by a factor of 2–3 and resulting in a twofold increase of the radiated power. In TEXTOR, instrumented dust holders with 1–45 mg of dust are exposed in the scrape-off layer 0–2 cm radially outside of the last closed flux surface in discharges heated with neutral beam injection (NBI) power of 1.4 MW. At the given configuration of the launch, the dust did not penetrate the core plasma and only moderately perturbed the edge plasma, as evidenced by an increase of the edge carbon content.

1. Introduction

Dust is commonly found in magnetic fusion devices [1–10]. Dust particulates found in tokamaks and stellarators range in size between ~ 10 nm and a few hundred μm [1,3–8]. Chemical composition of dust is determined mainly by the materials constituting the plasma facing components (PFCs), though dust may also contain plasma fuel elements (hydrogen isotopes) and radioactive elements generated by neutron bombardment of PFCs and dust. Dust production mechanisms in machines with carbon-based PFCs include flaking of redeposited layers, brittle destruction of graphite, arcing, agglomeration from supersaturated vapor, and growth from hydrocarbon molecules [6]. In machines with metallic PFCs loss of melt layer may be a major contributor to dust formation. Disruptions, edge localized modes (ELMs) and other transient events result in increased dust production.

In most contemporary machines dust is generally of little concern from an operational or safety standpoint. However, in superconducting devices with long pulse duration, such as LHD stellarator and Tore Supra tokamak, dust and debris have been observed to terminate discharges [11,12]. Dust is likely to be a greater concern in next-step devices such as ITER [5], where dust generation is expected to increase by several orders of magnitude due to the increased duty cycle and higher magnitude of particle and power fluxes deposited on the PFCs. Dust production and accumulation present potential safety issues for ITER by contributing to tritium inventory rise and leading to radiological and explosion hazards. The total in-vessel dust inventory in ITER will be limited to 1000 kg to ensure that environmental releases stay below the design limits in the case of the worst credible accident. A lower administrative limit of 670 kg has been proposed to take account of measurement uncertainties [13]. The enhanced chemical activity of dust at high temperatures is more restrictive, since in the case of an in-vessel coolant leak hot Be and C dust can react with

steam/water causing hydrogen generation and (in the case of simultaneous air ingress) explosion hazard. Thus a limit of 11 kg for Be and 15 kg for C dust on hot surfaces is being considered. More projections of dust production and accumulation rates based on experience from existing tokamaks and disruption simulators are needed. In addition, dust penetration of the core plasma can cause undesirably high impurity concentration and degrade performance. Allowable tungsten concentration for sustaining burning plasma in ITER is below 0.001%. This may result in a much stricter operational dust limit on plasma-exposed surfaces than that dictated by the safety considerations. Thus, studies of the dust transport and dynamics are important. Here we report studies of naturally occurring and artificially introduced dust in DIII-D and TEXTOR.

2. Studies of Naturally Occurring Dust in DIII-D

2.1. In-vessel dust inventory and evidence of various dust-forming processes

DIII-D [14] is a tokamak with major and minor radii of 1.67 m and 0.67 m. It has two poloidal divertors at the top and bottom of the vacuum vessel and can be operated in lower single null (LSN), upper single null (USN), double null (DN) and wall-limited magnetic configurations. Divertor and main chamber wall surfaces are lined with graphite tiles. Therefore, dust in DIII-D is predominantly carbon (fragments of graphite and redeposited hydrocarbon films). Dust collection has been performed in DIII-D during entry vents [3]. The median diameters of the collected dust samples ranged between 0.46 and 1.0 μm . The total in-vessel dust inventory was estimated to be between 33–120 g [3]. However, this estimate included dust found underneath the divertor tiles and was very likely dominated by the dust resulting from degradation of GRAFOIL® compliant layers under the tiles. Total amount of dust on the divertor surfaces was estimated at ~1.1 g [15]. Evidence of various dust-forming

processes is found during vents. Shown in Figure 1 are photographs of the upper divertor baffle tiles with exfoliating redeposited layers (a), upper divertor target tiles with strongly eroded leading edges (b), main chamber wall tiles with arc traces (c), and outboard bumper limiter tiles with thermal stress induced cracks and eroded edges of bolt holes (d). Approximate locations of the corresponding tiles in the poloidal cross-section of DIII-D are shown in Figure 2(b).

2.2. Diagnostic arrangement

Dust diagnostics in DIII-D include 2 dimensional (2D) imaging by cameras, scattering of laser light, and spectroscopic diagnostics [16]. Cameras allow recording individual particle trajectories and estimating the particle velocities; however, particle size is difficult to determine. Mie scattering from Nd:YAG lasers of the Thomson scattering system allows estimation of size of small particles (comparable to or smaller than the laser wavelength), and measuring dust size distributions and dust density in the plasma [17-20]. Spectroscopic diagnostics generally do not resolve individual dust particles, but can provide an indirect evidence of dust presence in the plasma and elemental information of the dust [16].

Arrangement of the diagnostics used for dust detection in DIII-D is shown in Figure 2. Shaded areas represent camera views: (1) fast framing camera [21], (2) tangential divertor TVs [22], (3) DiMES TV. Dots in (a) show views of spectroscopic diagnostics: (4) multichannel divertor spectrometer (MDS) [23], (5) filterscopes (telescopes with spectral line filters coupled to photo multipliers) [24]. MDS lines of view are shown in (b). Outermost viewing volumes of the core (6) and divertor (7) Thomson scattering systems are marked in (b). The location of the divertor material evaluation station (DiMES) (8) that allows insertion of material samples in the lower divertor [25] is marked in (a) and (b). A poloidal cross-section of a last closed flux surface (LCFS) of a LSN equilibrium with DiMES in the private

flux region is shown in (b). Locations of the inner and outer strike points (ISP and OSP) are marked by arrows.

A Thomson scattering system based on 8 Nd:YAG lasers is used primarily for the measurements of the electron density and temperature profiles [26]. Each laser produces pulses of about 10 ns duration at a 20 Hz repetition rate with a total energy per pulse of 0.5 J. The vertical core system has four collinear lasers, while the divertor system has a single laser. Light scattered from multiple positions along the laser path inside the plasma is collected by an optical system located outside the vacuum vessel and directed to polychromators, each with 6 detectors at different wavelengths. Viewing volumes are typically 1 cm in height and 5 mm in diameter. Non-shifted detector channels at the laser wavelength of 1064 nm allow for detection of light scattered by the dust particles. Signals from large particles cause saturation of the non-shifted channels, but some of them can be resolved by detectors with narrow band filters centered at 1062 nm which have an extinction factor of $\sim 10^{-2}$ at the laser wavelength. More detail on dust detection by the Thomson scattering system is available in Ref. [17]. Because of the short laser pulse duration and small viewing volume, dust observation rates are low, only a few events per discharge or less. Nevertheless, statistical analysis of the data provides an estimate of the total dust content in the edge and SOL plasmas, and allows establishing trends in dust production rates. Dust size can be estimated from the amplitude of the scattered signal detected. An analysis using a Mie scattering model and taking particle ablation by the laser into account has put the detectable particle size within the range of 0.16–1.6 μm in diameter [18].

Larger dust particles are detected by optical imaging with cameras. A number of standard frame rate CMOS and CID cameras and a fast framing CMOS camera are available on DIII-D (figure 2). A tangential view of the lower divertor [figure 2, view (2)] is split between two standard rate (60 images/s) CID cameras (“tangential TVs” [22]). Spatial resolution of both

tangential TV's is about 1.5-2.0 cm. A standard rate CMOS camera ("DiMES TV") views vertically down into the lower divertor [figure 2, view (2)] with a spatial resolution of about 1.5 mm. A fast framing CMOS camera (Phantom 7.1) [21] has a tangential view of the outboard chamber wall [figure 2, view (1)] with a spatial resolution of about 5 mm. The camera has a framing rate of up to 26 000 frames/s at 256×256 pixel resolution. All cameras have remotely changeable filters. Dust particles are occasionally observed with line filters such as D_{α} , CIII, etc., but most dedicated dust observations are performed either in full light or with Kodak Wratten 89B infrared filters, which block wavelengths below 700 nm. The fast camera has an inherently higher contrast ratio for moving incandescent objects, and therefore can resolve smaller and faster moving particles than standard rate cameras. As a result, the dust observation rate using the fast camera is much higher than that of the standard cameras.

2.3. Dust observations during "normal" plasma operations

During plasma operations on DIII-D, dust is present in the scrape-off layer (SOL) and edge plasma. Statistical average of the submicron dust density can be determined from the scattering data. The dust density is near the detection limit at the last closed flux surface (LCFS) and increases with distance into the SOL [17,19]. More dust is observed in high confinement mode (H-mode) with ELMs than in low confinement mode (L-mode) or ELM-free H-mode. Correlation of increased dust production with the presence of large ELMs has been established [20]. Figure 3 shows SOL profiles of the dust density measured by Mie scattering in H-mode discharges with varying ELM size and frequency. Dust density increases with increasing ELM amplitude compared to discharges with similar stored energy and more frequent smaller ELMs. Dust density measurements ordered with respect to the ELM timing show that the dust density in the SOL rises to a peak within 10ms of the end of an ELM and decays with a halflife of approximately 60ms after an ELM [20].

EX/9-3

When the vacuum vessel walls are well conditioned and there are no major disruptions, standard cameras register only isolated dust events in their field of view (typically single digit numbers per discharge or less) while the fast camera typically observes between 10–100 events per discharge. Individual particles move at velocities of up to ~ 500 m/s. Breakup of larger particles into pieces is sometimes observed. A sequence of frames in Figure 4(a-d) shows two comparatively large and slow (probably tens of microns in size and tens of m/s in velocity) dust particles that first become visible in the outboard SOL (a). Though reconstruction of the exact trajectory from a 2D image is impossible, it appears that the particles move towards the LCFS and develop large ablation clouds (b). The lower particle decays first (c), and the upper one follows (d). These data were taken by the fast camera without a filter, at 2000 frames/s. The total time between frames (a) and (d) is ~ 60 ms, and time between individual frames varies between 8–10 ms.

Collisions of dust particles with PFCs are sometimes observed. The sequence of frames in Figure 4(e-h) illustrates a large and rather fast (~ 500 m/s) particle colliding with the outboard chamber wall. On the order of a hundred of observable smaller particles are released following the collision [Fig 4(h)]. Whether these particles were fragments of the impinging particle or some of them originated from the wall remains an open question. If very fast (10 km/s and above) dust particles are present, their collisions with PFC surfaces may create craters hundreds of times larger in diameter than the original particle size [9]. However, no particles moving at velocities in excess of 1000 m/s have yet been observed in DIII-D, and no craters characteristic for impacts of such particles have been found on the PFCs.

2.4. Dust generation by disruptions

Disruptions cause transient heat loads on the PFC surfaces that can lead to dust production and mobilization. Statistical analysis of Mie scattering data shows increased dust

observation rates in plasma shots following discharges that ended with disruptions [19]. Release of dust from PFC surfaces during disruptions is directly observed by the fast-framing camera. A raw image of dust produced by a disruption with an upward-going vertical displacement event (VDE) is shown in Fig. 5(a). Figure 5(b) shows dust trajectories traced for ~ 8 ms after a similar disruption. The median velocity of these particles is 100 m/s, and particles with velocities as high as 280 m/s are observed. It is impossible to say whether the dust released following a disruption is actually “produced” by the disruption itself (by putting thermal stress on the graphite surface or re-deposited films), or it is loose dust accumulated at the surfaces during normal operations that gets mobilized. In any case, the trajectories and velocities of the dust particles observed following disruptions are inconsistent with a mere gravity fall following mechanical shaking of the vacuum vessel. Downward-going VDE disruptions often result in dust particles flying upwards. This is illustrated in Fig. 5(c,d), showing two consecutive fast camera frames obtained with CIII filter and 10 ms integration time. The dust particles are released at the bottom of the vessel and move upwards with velocities in excess of 100 m/s.

2.5. Dust observations following entry vents

It is possible that a large part of the dust inventory in DIII-D is created by in-vessel activities during entry vents. Indeed, dust observation rates after vents are significantly higher than during “normal operations”. In the first 2–3 plasma discharges after an entry vent, standard rate cameras detect hundreds of particles and the fast camera detects thousands of particles in each discharge. Figure 6 shows examples of dust tracks observed by the tangential TV (a) and DiMES TV (b). Both frames are taken in full light integrated over 16.6 ms. After about 15 discharges dust is virtually gone during the stationary portion of a discharge, and appears at much reduced levels during the plasma initiation and termination

phases. After a few days of plasma operations (about 70 discharges) dust levels are further reduced to the “normal operations” rates.

2.6. Estimation of the dust size from camera data

In principle, if chemical composition and the local plasma parameters at the location of a dust particle are known, one can relate the intensity of thermal radiation from a particle to the particle size [7,27]. If an absolute *in situ* calibration of the camera sensitivity is available, it may be possible to determine the particle size from the intensity of a recorded image, however, in practice this task is extremely complicated. Luminosity of a dust particle is a very strong function of the local plasma density, n_e , and electron temperature, T_e [7,27]. Since gradients of n_e and T_e with typical e-folding lengths of 2–8 cm exist in the SOL [28], with a 2D view it's practically impossible to determine a particle position with sufficient accuracy for a reasonable size estimate. In addition, line radiation from the ablation cloud around a particle can contribute significantly to or even dominate the detected radiation [Fig. 2(c)]. An alternative approach for determination of a particle size from camera data involves comparison of a particle life time in the plasma with a theoretical ablation rate of a carbon sphere [27]. This method has been recently applied in DIII-D [29]. Life times of the dust particles ablated by ELM filaments propagating outwards across the outboard SOL were measured from the fast camera images. Plasma parameters inside the ELM filaments were assumed to be comparable to those at the top of H-mode edge pedestal (typically $n_{e,ped} = 3 \times 10^{13} \text{ cm}^{-3}$ and $T_{e,ped} = 400 \text{ eV}$). Most dust particles are destroyed within a single ELM, however, the largest observed particles survive up to 12 ELMs. A distribution of inferred dust size was constructed based on 2,330 particles detected by the fast camera during H-mode operation in 12 plasma discharges [29]. The inferred particle diameters were between $\sim 3 \text{ }\mu\text{m}$

and ~ 1 mm. The upper end, however, may be an overestimate, since the decay of the density and temperature inside ELM filaments propagating through the SOL was neglected, so the ablation rates were probably overestimated.

2.7. Correlation of the dust velocity and size

Correlation of the dust velocity with the inferred dust size has been studied [29]. From the camera data it's only possible to measure a 2D velocity projection on to a plane perpendicular to the viewing direction, which is a lower limit on actual 3D velocity magnitude. Figure 7 shows the projected velocities versus the inferred particle radii. The vertical bars represent the standard deviation of velocities for particles in each radius bin. The horizontal bars show variation in the inferred radius when n_e and T_e are varied by a factor of 2 from the pedestal values. An inverse dependence with a slope close to $R_d^{-1/2}$ (dashed line shown for comparison in Fig. 7) has been found. This is consistent with modeling by the DustT code [30], which predicts that smaller particles experience faster acceleration by the ion drag force. The $R_d^{-1/2}$ scaling of the dust velocity is also predicted by a simplified one-dimensional uniform plasma model [30]. The data point in Fig. 3 marked with a solid square comes from injection of pre-characterized graphite dust [Section 3.1]. The fact that it is shifted towards the smaller particle size compared to the rest of the points is another indication that the inferred particle sizes may be somewhat overestimated.

2.8. Large flakes leading to discharge termination

As mentioned in Section 1, discharge termination by dust and flake injection has been reported in LHD and Tore Supra. Similar events, though extremely rare, have been observed in DIII-D. Figure 8(a-h) shows a sequence of frames from the divertor tangential TV

illustrating a time history of a comparatively large object ("UFO") moving through the plasma and eventually causing a disruption [Fig. 8(h)]. The UFO first enters the camera field of view moving close to the divertor floor (a-b), then it appears to strike the floor and change the direction of motion (c). The object also starts gyrating (d-g). An object of this size can not possibly be magnetized, so this must be a solid body rotation around the center of mass, and the apparent spiral pattern must be due to a non-uniform radiation from the surface. The UFO was probably either a large flake similar to those shown in Fig. 1(a) or a piece of graphite. Strong increase of the carbon radiation from the plasma core just before the disruption confirms that the UFO consisted mostly of carbon.

2.9. Interaction of NBI neutrals with dust particles

Direct interaction of the energetic neutrals from the Neutral Beam Injection (NBI) heating system with dust particles has been observed. Figure 9 shows dust particles observed by the fast camera in front of the NBI injection port 1 ms before (a), during (b) and 2 ms after a NBI pulse. The heating pulse duration was 10 ms, amplitude 2.5 MW. During the pulse dust particles glow significantly brighter than before or after it, presumably due to the increase of the particle surface temperature caused by the neutral heating. The effect may be partly due to the increase of the local plasma temperature. However, the particles that appear to be inside the NBI port, where there is no or very little plasma due to a short connection length, become brighter as well. Therefore, it is likely that the particles are heated directly by the NBI neutrals.

2.10. Dust acceleration by plasma flows

Plasma flows accelerate dust particles via ion drag force. Dust dynamic simulations [7,27] show that the drag force is often the dominant force acting on a dust particle in a plasma. Figure 10 presents evidence of the effect of divertor flows on a dust particle trajectory. Shown is a dust particle track recorded by DiMES TV with CD filter (430.5 nm center, 3.5 nm bandpass), integrated over 33 ms. Locations of the outer and inner strike points (OSP and ISP) are marked by dashed lines. The expected plasma flow direction in the divertor is always along the field lines toward the plate. Since the vertical component of the magnetic field changes sign at the ISP (pointing down radially outwards of the ISP and up inwards of it), magnetic field line pitch changes as well. For the conditions of Figure 10, the expected toroidal component of the flow is directed from left to right in the private flux region (PFR) and from right to left inwards of the ISP. The track originates near the OSP and traverses the PFR without significant change in direction. It appears that the flow in the PFR is not sufficiently strong to affect the particle trajectory. However, when part of the original particle breaks off and then splits in three pieces, these smaller particles do get accelerated in the expected direction of the PFR flow. The larger part of the original particle continues to travel toward ISP (small change in the direction should be due to the momentum conservation after the split). Once it crosses the ISP, it begins to get accelerated in the opposite direction, which is the expected flow direction in that region. This example shows that dust particles may be potentially used for diagnostic of the plasma flows, if not in magnitude, then at least in the direction. For a known size particle in a known density and temperature plasma, it should be possible to estimate the flow velocity as well [31].

3. Experiments with Intentionally Introduced Dust in DIII-D and TEXTOR

3.1. Experiments with carbon dust introduced in the lower divertor of DIII-D

Injecting pre-characterized dust from a known location can be used to calibrate diagnostic measurements and benchmark modeling of dust dynamics and transport. Migration of carbon dust has been studied in DIII-D by introduction of micron-size graphite dust in the lower divertor [32]. The dust used in most of the experiments was supplied by Toyo Tanso Co. Figure 11 shows an optical microphotograph (a), a scanning electron microscope (SEM) image (b), and a volume (mass-based) size distribution of the dust. The median diameter is ~6 microns.

A few experiments have been performed. In each case, 25–40 mg of dust was placed on a graphite DiMES sample holder. To avoid dust being blown away during sample handling and pump-down, a suspension of dust in ethanol was applied to the holder and allowed to dry. Upon drying, dust formed a smooth uniform layer 0.1–0.5 mm thick. The holder was inserted in the lower divertor, flush with the tile surface. The dust was then exposed to ELMy H-mode discharges with strike points swept across the divertor floor. The typical discharge parameters were: toroidal magnetic field, $B_T = 2\text{--}2.1$ T, plasma current, $I_p = 1.1\text{--}1.4$ MA, NBI heating power, $P_{\text{NBI}} = 4.5\text{--}8.5$ MW, line-average plasma density, $\bar{n}_e = 4.5\text{--}6.0 \times 10^{19} \text{ m}^{-3}$. In the early part of the discharge the holder with dust was kept in the private flux region (as shown in Fig. 12(a), black separatrix), then the outer strike point was swept radially inward over the dust. Following a brief exposure (~0.1 s) at the OSP, part of the dust was injected into the plasma. A frame from the tangential divertor TV with infrared filter shows a direct view of the injection [Fig. 12(c), the DiMES location is marked by a circle]. About 1.5%–2.0% of the total dust carbon content ($2\text{--}3 \times 10^{19}$ carbon atoms, equivalent to a few million dust particles) penetrated the core plasma, raising the core carbon density by a factor of 2–3

and resulting in a twofold increase of the total radiated power [Fig. 12(b)]. Temporal evolution of the normalized carbon density profile (versus the normalized radius) measured by charge exchange recombination spectroscopy (CER) [33] following the dust injection is shown in Fig. 12(d). When the carbon concentration reaches its maximum around 250 ms after the beginning of the dust injection (at ~3350 ms), n_C/n_e between $\rho=0.85$ and $\rho=0.9$ rises to over 16%, meaning that in that region the plasma is almost purely carbon.

Following the dust injection, individual dust particles were observed moving at velocities of 10–100 m/s, with trajectories elongated in the toroidal direction [Fig. 12(c)], consistent with acceleration by the ion drag force [Section 2.10]. The fast framing camera observed large amounts of injected dust in the outboard SOL 90° or more toroidally away from the injection point [16]. This confirms that injected dust becomes highly mobile and travels far away from the point of origin in both toroidal and poloidal directions. During the dust injection, MDS spectrometer observed a strong increase in the thermal continuum emission radiation at DiMES location. Concurrent increases in CII emission, C2 dimer emission, and CI atomic emission were also observed. This observation may be useful for designing novel survey diagnostics for carbon dust in tokamak divertor and SOL plasmas [16].

An injection of diamond dust of finely calibrated size between 2–4 microns was recently performed. Dust from the injection was observed by the fast camera, but required digital background subtraction to be resolved. Therefore, it was experimentally demonstrated that 4 micron dust is about the smallest that can be resolved by the fast camera in the existing setup at DIII-D, consistent with the estimates of Ref [29].

3.2. Experiments with carbon dust introduced in the SOL of TEXTOR

Dedicated experiments with dust have started recently in TEXTOR. Pre-characterized carbon dust similar to that used in DIII-D [Fig. 11] was introduced in amounts ranging from 1 to 45 mg on instrumented dust holders. Schematic of the experimental setup is shown in Figure 13(a). The holders were mounted on the spherical test-limiter and exposed one by one in the SOL of TEXTOR using the Limiter Lock transport system at the bottom of the vacuum vessel. Figure 13 shows a view of the limiter with a dust holder (b), and a close-up of the exposed holder with remaining dust (c). Three holders with different amounts of dust were exposed during repetitive NBI-heated discharges with $P_{NBI} = 1.4$ MW and $\bar{n}_e = 2.5 \times 10^{19} \text{ m}^{-3}$, at the radial locations from 0 to 2 cm outside of the LCFS. Local plasma parameters near the dust launch locations were $n_{e,loc} \sim 2\text{--}2.5 \times 10^{18} \text{ m}^{-3}$ and $T_{e,loc} \sim 30\text{--}35$ eV. During the exposure of instrumented holders the dust launch occurred either in the beginning of the discharge at $t = 0$ s or at $t = 1.5$ s when NBI injector was activated. Analyses of recorded video sequences from a downward-looking camera without a filter [Fig. 14(a)] evidenced the launch of dust in a direction perpendicular to the toroidal magnetic field. The motion of the dust was caused by the Lorentz force due to the thermoelectron current emitted by the hot dust particles in the same way as it was earlier observed in TEXTOR during experiments with tungsten melt layer formation [34].

An extensive set of plasma diagnostics was used to investigate the motion of the dust in TEXTOR plasmas and its impact on the core performance. The diagnostics involved the Thomson scattering system, operating both in active and in passive (without laser irradiation) modes, fast cameras and a set of edge and core spectroscopes including the high efficiency extreme ultraviolet overview spectrometer system HEXOS [35]. After exposure of the dust samples, careful analysis of the data from the core spectroscopy systems, fast cameras and Thomson scattering system did not reveal any measurable change of the core performance.

The amount of dust launched during TEXTOR discharges was estimated by weighting the dust holders with and without dust before and after the exposures. In the 4 discharges where the dust launch occurred, the total amount of dust lost from the holders was about 43 mg, which corresponds to $\sim 2.2 \times 10^{21}$ carbon atoms. Given the fact that the detection limit of the core diagnostics is about 10^{13} particles, the conclusion can be made that the dust didn't enter the core of TEXTOR.

At the same time, analyses of the data from edge spectroscopy did reveal clear signals resulting from the dust launch. A 2D image recorded by a horizontally-looking camera equipped with CIII filter is shown in Fig. 14(b). This picture was made during discharge 106265 at a time $t = 1510$ ms, i.e. immediately after the NBI start. Analysis of the edge spectroscopic data showed that the carbon concentration in edge plasmas increased from around 3% to up to about 6% during the launching events. This increase corresponds to $\sim 10^{17}$ additional carbon atoms in the edge plasma. Therefore, less than 0.01% of the launched dust carbon content ended up in the plasma. The present understanding is that the major part of the injected dust was deposited on the adjacent PFC surfaces immediately after the launch.

4. Discussion

Dust generally presents no problem for DIII-D operations, except immediately after entry vents. From Mie scattering measurements during “normal operations”, it is concluded that even at the highest dust densities estimated total carbon content of the dust is less than a few percent of the plasma carbon impurity content [17,18]. Based on this result, we conclude that submicron dust is not a major impurity source in DIII-D. Larger size particles are too scarce in numbers during “normal operations” to significantly contribute to the impurity sources.

However, in very rare occasions large flakes or debris fall into the plasma and may cause a disruption.

Proposed dust inventory accounting method for ITER is based on the measurements of the net erosion and assumption that 100% of the eroded material is converted into dust [13]. The latter assumption may be too conservative: the fraction of the eroded material converted into mobilizable dust may be in fact substantially smaller. It would be useful to estimate the corresponding conversion fraction for DIII-D. However, using the total in-vessel dust inventory for such an estimate could be misleading because of the dust and debris generated by the processes unrelated to the plasma operations (GRAFOIL® debris under tiles, etc.). The measured amount of ~1.1 g of dust on the lower divertor surfaces [15] is probably more representative of the PMI-created dust inventory, though it does not account for the dust that may fall into the gaps between tiles. We therefore assume that the amount of dust created during plasma operations in DIII-D over a 1 year experimental campaign (10-15 weeks of operations, 7000-10000 plasma seconds) is between 1 and 10 g.

Net erosion of the lower divertor tiles over an experimental campaign has been measured by profilometry [36]. The net erosion in the outer part of the divertor was 12.4 cm^3 , while in the inner part a net deposition of 9.7 cm^3 was measured. Thus the total net erosion in the lower divertor was 2.7 cm^3 . For the graphite density of 1.75 g/cm^3 , we get 4.7 g of eroded graphite. This is comparable to the dust inventory estimated above. Additional net erosion may occur in the upper divertor and at the main chamber wall. Because of the ambiguity of both the total dust inventory and the total net erosion estimates, making an accurate estimate of the fraction of the eroded material converted into dust does not seem possible. From our data, it can be anywhere between 10 and 100%.

We can also try to estimate (roughly at least) how much dust is produced by some individual mechanisms discussed above. For example, a typical disruption results in up to

~1000 dust particles within the fast camera view, corresponding to ~10000 particles for the whole vessel. This corresponds to between 0.01–1 mg of carbon, depending on the dust size, which is hard to determine from the camera data. Taking the upper bound estimate, disruptions in DIII-D may produce up to ~1 g of dust over a 15 week experimental campaign. This is comparable to the amount of dust on the divertor surfaces, so disruptions can not be ruled out as a major contributor to dust production in DIII-D.

Observed velocities and trajectories of the dust particles in DIII-D are in qualitative agreement with modeling by the DustT code [7,27,30]. Acceleration of the dust particles by the plasma flows and toroidal elongation of the dust trajectories predicted by the modeling are observed experimentally [Section 3]. The range of the dust velocities predicted by the code is in good agreement with the camera data. Other features are also reproduced. Figure 15 shows poloidal projections of a few dust trajectories calculated by the DustT code for DIII-D geometry and edge/SOL plasma parameters. The modeling shows that dust originating in the lower divertor can migrate into the main chamber (e.g. the trajectory marked by an arrow in Fig. 15). This is indeed observed in experiments with the dust intentionally introduced in the lower divertor [Section 3.1].

5. Summary and Conclusion

In summary, progress has been made in characterization of naturally occurring and artificially introduced carbon dust in DIII-D and TEXTOR. Micron size dust has been shown to be highly mobile, travelling at velocities of up to hundreds of m/s. Dust does not present operational concerns in DIII-D except immediately after entry vents. Disruptions and ELMs produce notable amounts of dust in DIII-D. These impulsive sources of dust remain a concern for ITER, where wall loads from ELMs and disruptions will be large compared to those in

DIII-D. Experiments with artificially introduced dust in DIII-D showed that dust can migrate from the lower divertor into the main chamber and contribute to the core plasma contamination with impurities. In contrast, the first experiment with artificially introduced dust in TEXTOR demonstrated that, at the given configuration of the launch, the dust did not penetrate the core plasma and only moderately perturbed the edge plasma, as evidenced by a moderate increase of the edge carbon content.

Acknowledgments

This work was supported in part by the US Department of Energy under DE-FG02-07ER54917, DE-FC02-04ER54698, DE-AC52-07NA 27344 (with LLNL), DE-AC02-76CH03073, and DE-AC04-94AL85000.

References

- [1] R. Behrisch, *et al.*, J. Nucl. Mater. **76-77**, 437 (1978).
- [2] Goodall, D. H. J., J. Nucl. Mater. **111-112**, 11 (1982).
- [3] Carmack, W. J., *et al.*, Fusion Eng. Des. **39-40**, 477 (1998); W.J. Carmac, *et al.*, Fusion Eng. Des. **51-52**, 477 (2000).
- [4] Rubel, M., *et al.*, Nucl. Fusion **41**, 1087 (2001).
- [5] Federici, G., *et al.*, Nucl. Fusion **41**, 1967 (2001).
- [6] Winter, J., Plasma Phys. Control. Fusion **46**, B583 (2004).
- [7] Pigarov, A. Yu., *et al.*, Phys. Plasmas **12**, 122508 (2005).
- [8] Wang, Z., *et al.*, *New Aspects of Plasma Physics*, edited by P. K. Shuk la, L. Stenflo, and B. Eliasson (World Scientific, Singapore, 2008), pp. 394–475.
- [9] Ratynskaia, S., *et al.*, Plasma Phys. Control. Fusion **50**, 124046 (2008).
- [10] Krashennnikov, S.I., *et al.*, Plasma Phys. Control. Fusion **50**, 124054 (2008).
- [11] Saito, K., *et al.*, J. Nucl. Mater. **363-365**, 1323 (2007).
- [12] [Tore Supra], these proceedings.
- [13] S. Ciattaglia, *et al.*, Proceedings of the Symposium on Fusion Technology, Rostock, 15-19 Sept 2008. To be published in Fus. Engin. & Des. (2009).
- [14] Luxon, J. L., Nucl. Fusion **42**, 614 (2002).
- [15] Sharpe, J.P., private communication (2008).
- [16] Rudakov, D.L., *et al.*, Rev. Sci. Instrum. **79**, 10F303 (2008).
- [17] West, W.P., *et al.*, Plasma Phys. Control. Fusion **48**, 1661 (2006).
- [18] Smirnov, R.D., *et al.*, Phys. Plasmas **14**, 112507 (2007).
- [19] West, W.P., Bray, B.D., J. Nucl. Mater. **363-365**, 107 (2007).

- [20] Bray, B.D., *et al.*, *Proc. 18th Plasma Surface Interactions Conf.*, Toledo, 2008; also “Correlation of submicron dust production in DIII-D to impulsive wall heating from ELMs”, *J. Nucl. Mater.*, in press.
- [21] Yu, J.H., *et al.*, *Phys. Plasmas* **15**, 032504 (2008).
- [22] Groth, M., *et al.*, *Rev. Sci. Instrum.* **74**, 2064 (2003).
- [23] Brooks, N. H., *et al.*, *Rev. Sci. Instrum.* **63**, 5167 (1992).
- [24] Colchin, R. J., *et al.*, *Rev. Sci. Instrum.* **74**, 2068 (2003).
- [25] Wong, C. P. C., *et al.*, *J. Nucl. Mater.* **258-263**, 433 (1998).
- [26] Carlstrom, T. N., *et al.*, *Rev. Sci. Instrum.* **63**, 4901 (1992).
- [27] Smirnov, R.D., *et al.*, *Plasma Phys. Control. Fusion* **49**, 347 (2007).
- [28] Rudakov, D.L., *et al.*, *Nucl. Fusion* **45**, 1589 (2005).
- [29] Yu, J.H., *et al.*, *Proc. 18th Plasma Surface Interactions Conf.*, Toledo, 2008; also “Fast camera imaging of dust in the DIII-D tokamak,” *J. Nucl. Mater.*, in press.
- [30] Smirnov, R.D., *et al.*, *Proc. 18th Plasma Surface Interactions Conf.*, Toledo, 2008; also “Modeling of velocity distributions of dust in tokamak edge plasmas and dust-wall collisions,” *J. Nucl. Mater.*, in press.
- [31] Wang, Z. and Ticos, C. M., *Rev. Sci. Instrum.* **79**, 10F333 (2008).
- [32] Rudakov, D.L., *et al.*, *J. Nucl. Mater.* **363-365**, 227 (2007).
- [33] Burrell K.H., *et al.*, *Rev. Sci. Instrum.* **75**, 3455 (2004).
- [34] Sergienko, G., *et al.*, *J. Nucl. Mater.* **363-365**, 96 (2007).
- [35] Biel, W., *et al.*, *Rev. Sci. Instrum.* **77**, 10F305 (2006).
- [36] C.P.C. Wong *et al.*, *J. Nucl. Mater.* **196-198**, 871 (1992).

Figure captions

Fig. 1: Evidence of the dust-forming processes in DIII-D: exfoliating redeposited layers (a), erosion of leading edges (b), arc traces (c), thermal stress induced cracks (d). Poloidal location of the tiles is shown in Figure 2(b).

Fig. 2: Diagnostic arrangement on DIII-D: (1) fast camera, (2) tangential divertor TVs, (3) DiMES TV, (4) MD S, (5) filterscopes, (6) core Thomson, (7) divertor Thomson, and (8) DiMES. “A, B, C, D” in (b) show approximate locations of the corresponding tiles from Figure 1.

Fig. 3: Radial profiles of the dust density measured by Mie scattering in H-mode discharges with varying EML size and frequency.

Fig. 4: Time history of dust particles observed by the fast camera in the outboard DIII-D SOL. Shown are two particles entering SOL and disintegrating (a-d), and a particle colliding with the outboard wall (e-h).

Fig. 5: Fast camera images of dust released by upward-going (a,b) and downward-going (c,d) VDE disruptions.

Fig. 6: Dust observed after an entry vent by lower divertor tangential TV (a) and DiMES TV (b).

Fig. 7: Measured 2D dust velocity decreases with the dust size inferred from the ablation model [29]. The data point marked with a solid square is for pre-characterized injected dust [Section 3.1].

Fig. 8: Time history of a “UFO” leading to a disruption.

Fig. 9: Dust observed by the fast camera in front of the NBI injection port 1 ms before (a), during (b) and 2 ms after a NBI pulse.

Fig. 10: Effect of plasma flows on a dust particle motion.

Fig. 11: Optical microphotograph (a), SEM image (b), and a volume size distribution (c) of the graphite dust used in dust injection experiments in DIII-D and TEXTOR.

Fig. 12: Dust injection experiments in DIII-D: (a) dust exposure geometry; (b) temporal evolution of the discharge and plasma parameters; (c) dust injection observed by the tangential divertor TV; (d) temporal evolution of the normalized carbon density profile.

Fig. 13: Dust injection experiments in TEXTOR: schematic of the experimental setup (a); limiter with a dust holder (b); close-up of the exposed holder with remaining dust (c).

Fig. 14: Launch of dust at the beginning of NBI phase in TEXTOR (a); spectroscopic view of the dust launch (b).

Fig. 15: Poloidal projection of the dust trajectories modeled by DustT code for DIII-D geometry and plasma conditions.



Figure 1

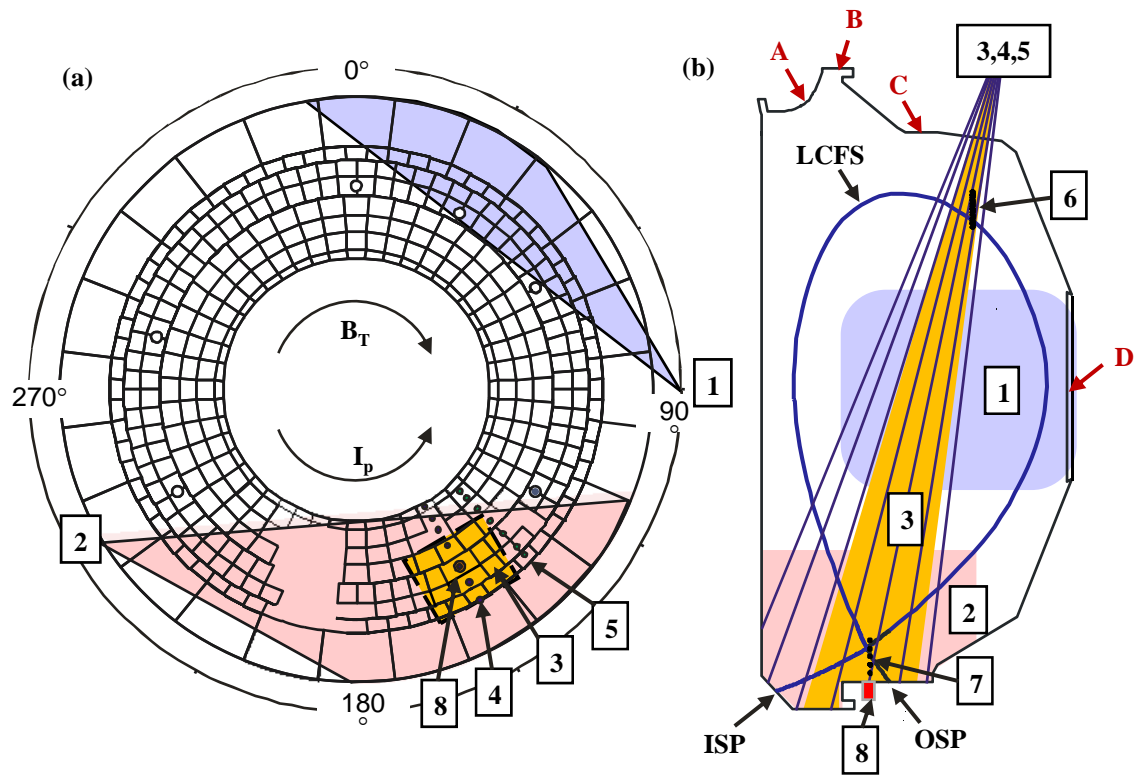


Figure 2

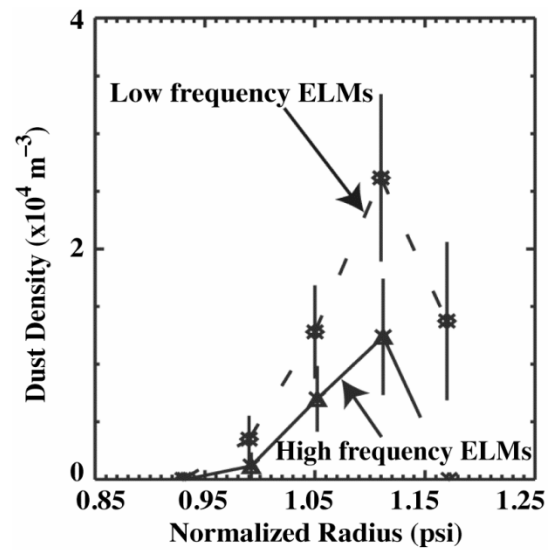


Figure 3

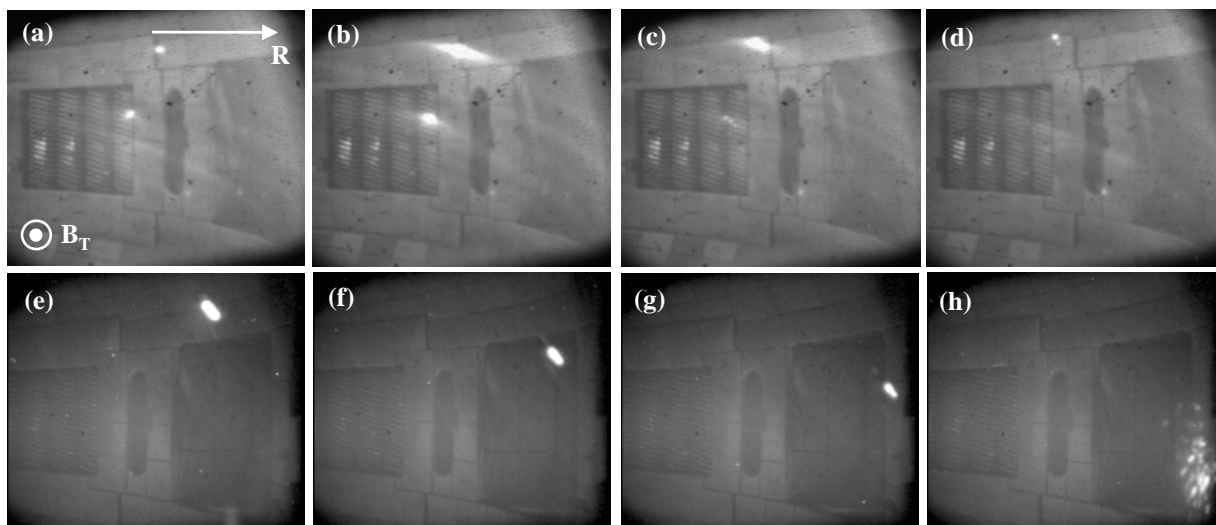


Figure 4

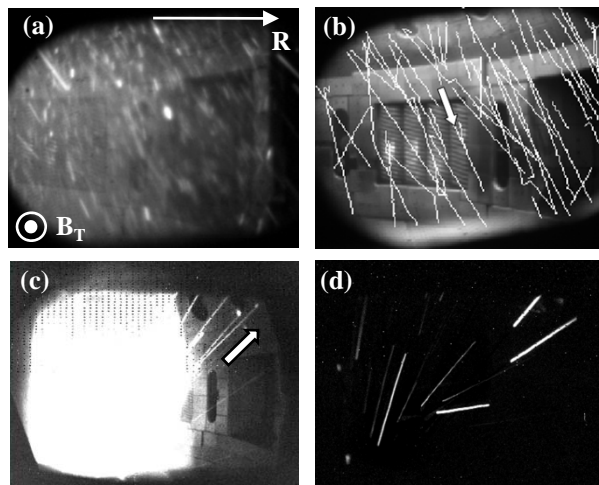


Figure 5

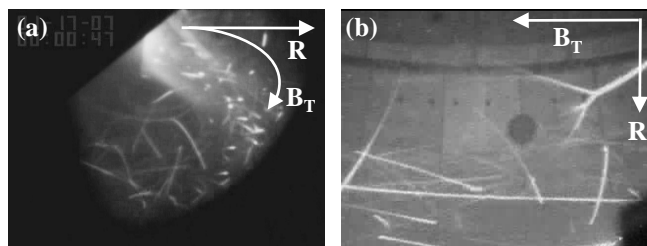


Figure 6

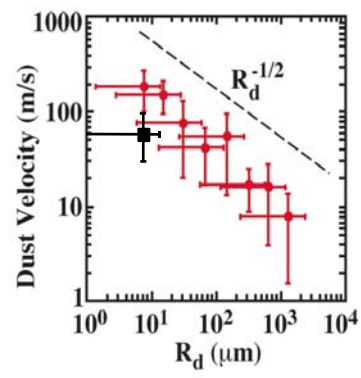


Figure 7

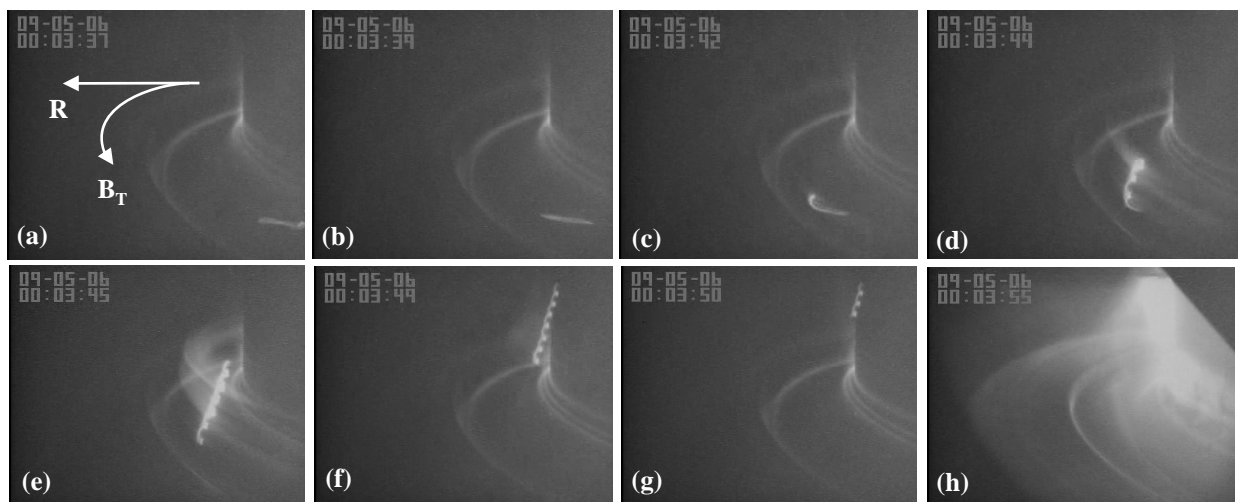


Figure 8

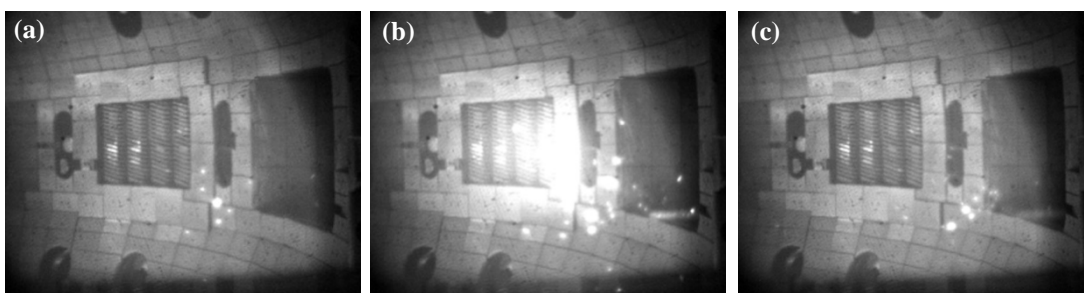


Figure 9

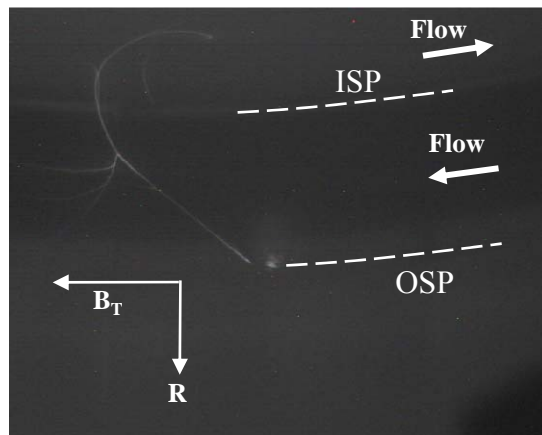


Figure 10

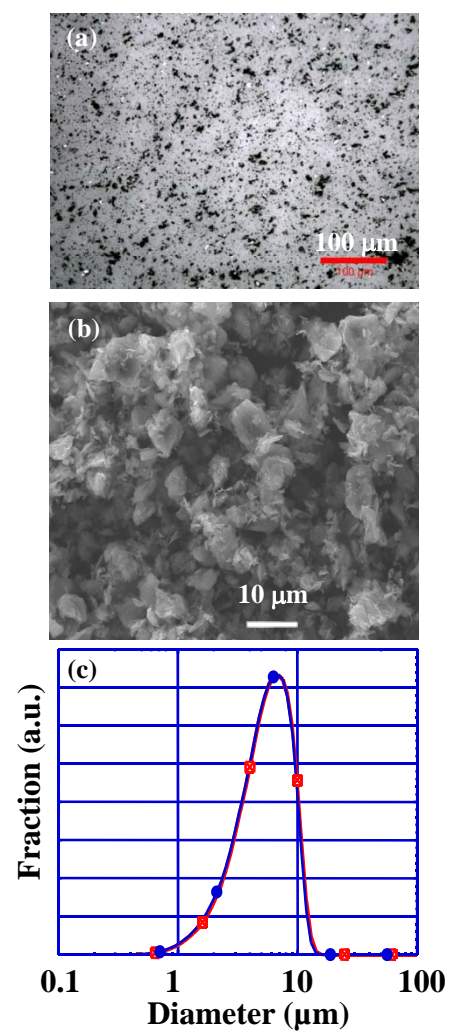


Figure 11

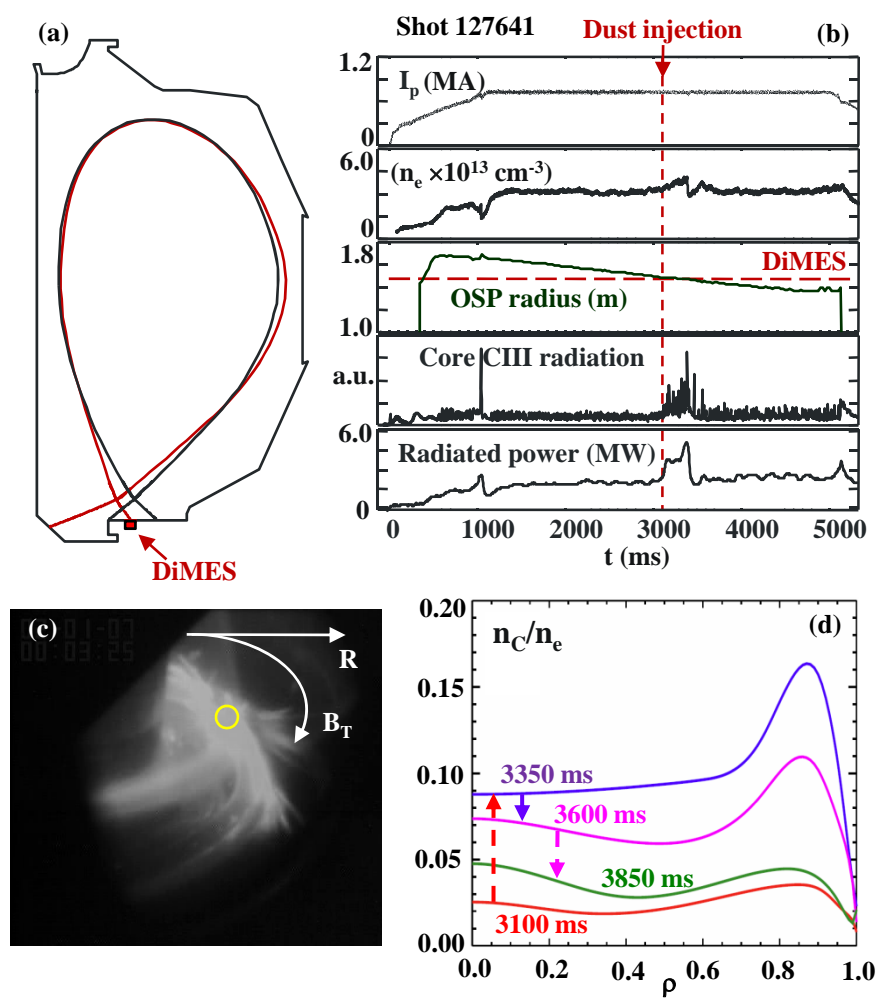


Figure 12

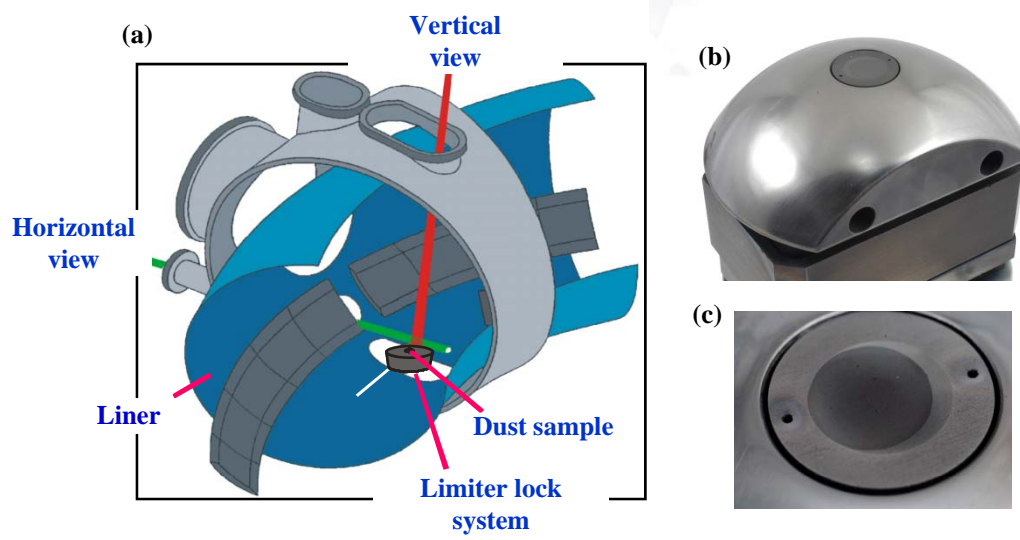


Figure 13

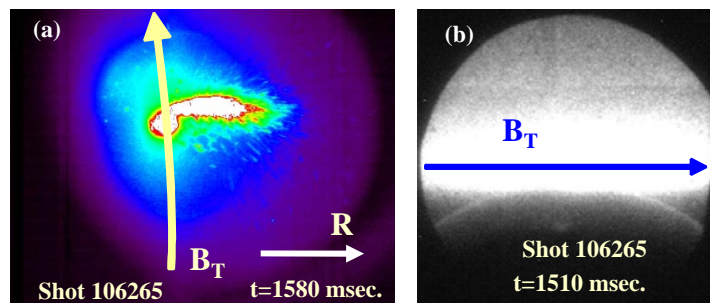


Figure 14

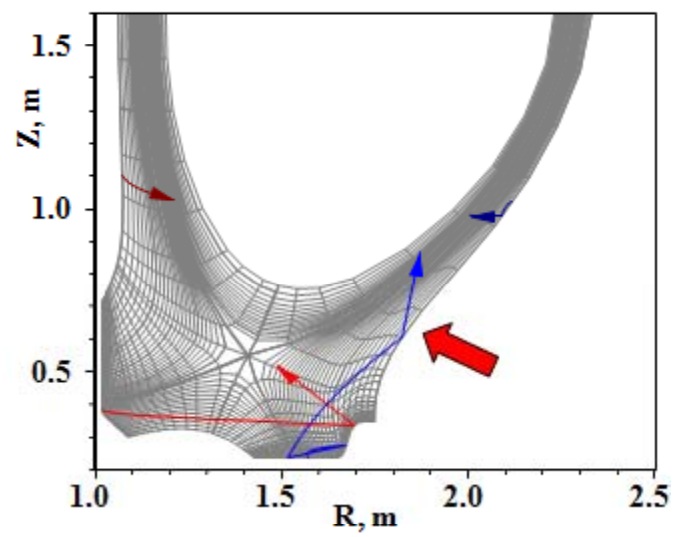


Figure 15